

Research Article

Experimental Investigation of Laws during Deformation of Circular Roadway in 10° Inclined Layered Rock

Xiaoming Sun,^{1,2} Qiang Han,^{1,2} Yingqi Zhang,³ Xin Liu,^{1,2} and Weili Gong^{1,2}

¹State Key Laboratory for Geomechanics & Deep Underground Engineering, Beijing 100083, China

²School of Mechanics and Civil Engineering, China University of Mining & Technology, Beijing 100083, China

³Lawrence Berkeley National Laboratory, Berkeley, CA 94720, USA

Correspondence should be addressed to Xiaoming Sun; sxmcmtd@163.com

Received 4 October 2016; Revised 10 April 2017; Accepted 12 April 2017; Published 18 May 2017

Academic Editor: Carlo Santulli

Copyright © 2017 Xiaoming Sun et al. This is an open access article distributed under the Creative Commons Attribution License, which permits unrestricted use, distribution, and reproduction in any medium, provided the original work is properly cited.

In order to analyze the deformation characteristics and mechanisms caused by high tectonic stress in gentle dip strata, a physical modeling with circular tunnel was designed. The model was constructed by the so-called “Physically Finite Elemental Slab Assemblage (PFESA)” to bring about the structural effect of the deep strata. The gravity was fixed while the lateral pressure increased step by step to mimic high tectonic stress. In order to observe the displacement in different area, the sketches of monitoring points and frame in the model surface were drawn down through video pictures in different periods and to be compared. For the sake of analyzing the deformation and failure mechanism of layers, rock structural mechanics models were set up for the left side and right side in the same stratum, respectively. For verifying the experimental phenomenon and its mechanism, infrared images were utilized based on the temperature variation mechanisms of material. Through systematic study, this paper enriches the research methods of model test and can provide a certain reference for practical engineering of similar conditions.

1. Introduction

With the decreasing shallow resources, mining industry starts to focus on extracting deep underground resources. The environment makes the deep rock mechanical characteristics and engineering responses very distinctive [1–4]. Rock stratum is much weaker in deep underground than it is at shallow depth due to the higher surrounding stress. Therefore the rock stratum is more prone to generate large deformation. Serious deformation can cause the roadway to narrow, hinder transport, and affect normal production [5].

The most widely used method is numerical simulation when analyzing the formation of deformation. References [6, 7] used numerical analysis to study floor heave and deformation in swelling ground under high humid condition; reference [8] revealed the way of water inflow in mine based on evaluating stress redistribution and strata failure; reference [9] used different numerical modeling techniques (continuum, discontinuum, and hybrid discrete finite element) to model the deformational behavior of coal strata. Although it is laborious to construct, physical modeling has been

indispensable and played a key role in understanding the mechanism of deformation and failure in deep roadway [10, 11]. A large-scale physical model can avoid scaling problems of parameters and variables, but is expensive to build. In recent years, a new physical modeling technique, that is, the Physically Finite Elemental Slab Assemblage (PFESA), has been proposed to construct large-scale geological physical models for mimicking stratified rock masses [12]. Although the Elemental Slabs are made of artificial materials, the physical and mechanical properties are similar to the real rocks. The PFESA uses specimen-sized rectangular plates—the Elemental Slabs, which can be put into mass production with a low cost. The expenses of constructing a large-scale physical model are largely reduced.

In this paper, the PFESA technique is used to build a large-scale geomechanical model to mimic deep gentle inclined stratified rock mass. A video camera and an infrared thermal imager are set up to observe the deformation and temperature variation of the model before and after excavation of the circular roadway under symmetrical loading. The measurements can help us understand the deformation

TABLE 1: Material properties of the real rocks.

Rock types	Volumetric weight (kN/m ³)	Compressive strength (MPa)	Elastic moduli (GPa)	Poisson's ratio	Friction angle (°)
Sandstone	26.55	63.98	25.77	0.151	33.71
Mudstone	25.78	43.78	21.01	0.127	36.35
Coal seam	13.50	26.15	4.51	0.358	40.07

TABLE 2: Material properties of the elementary slabs.

Dimensions (cm ³)	Simulated rock types	Ratio of water-gypsum	Volumetric weight (kN/m ³)	Compressive strength (MPa)	Elastic moduli (GPa)
40 × 40 × 3	Sandstone	0.8 : 1	14.68	6.748	1.28
40 × 40 × 2	Mudstone	1 : 1	11.25	4.663	0.94
40 × 40 × 1	Coal seam	1.2 : 1	8.40	3.382	0.81

mechanism in mechanical characteristic and energy-dissipation regimes.

2. Physical Model Construction

Deep rock masses in China coal mine can be generally divided into three categories, that is, sandstones, mudstones, and coal rocks [13]. The prototype of this test is also used in the previous experiments carried out at the State Key Laboratory for Geomechanics and Deep Underground Engineering at the China University of Mining & Technology, Beijing (CUMTB). Those rocks are taken from Qishan coal mine, Jiangsu Province. The rocks in the region are composed of these three types of rocks which is representative of China coal mine. The rock strata have a large inclination angle varying from 0° to 90° [12–18]. Among them is the contact alley in the north wing at the –1000 m level, whose structure of the strata is that the roof is sandstone, the body of excavation is coal, and the floor is mudstone; the inclined angle is 10° to 15°. In the process of excavation, phenomenon of floor heave and shrinkage of two sides are serious and in an asymmetric situation. The material properties of the real rocks are shown in Table 1.

The dimensions of the physical model are 1600 × 1600 × 400 mm³ and the roadway is designed as a circular space in the center of the model with the diameter of 300 mm. The geometric similarity factor is selected empirically as $C_l = 10$, which met the requirements in experimental system operating instruction of physical models in deep mine engineering. In addition, the physical model should also satisfy other similarity theories, including the stress similarity factor, defined as $C_\sigma = 10$; the volumetric weight similarity factor which can be derived by the relation:

$$C_\gamma = \frac{C_\sigma}{C_l} = 1. \quad (1)$$

The PFESA technique is employed here. This method utilizes assembly of rectangular plates which are made of artificial materials according to “similarity theory.” In order to simulate the inclined rock strata, large numbers of these slabs are

arranged at the specified orientation, which is 10° in this case. The elementary slabs (i.e., similarity material) in former tests carried out in CUMTB are cubic gypsum plates, as shown in Figure 1(a), which are produced based on different ratio of water-gypsum. The dimensions of the elementary slabs are 40 × 40 × 3 cm³, 40 × 40 × 2 cm³, and 40 × 40 × 1 cm³, respectively. The model had three strata in total, sandstone layers, coal seam, and mudstone layers, from top to bottom, which is illustrated in Figure 1(b). The material properties of the elementary slabs are reported in Table 2.

3. Loading Conditions and Test Procedures

The whole loading scheme of the test includes three processes: (1) process to establish the in situ stress conditions (i.e., initial condition before mining activities start); (2) simulated roadway excavation process; (3) process of adjusting lateral pressure until the model is damaged if the model had not failed after process (2).

In situ stress condition was established by applying horizontal load (to mimic the tectonic stress) and vertical load (to mimic the gravity of the overburden) on the model, in a plane stress state. The “Geological Disaster Simulation Testing Machine whose model type is YDMC-C” was equipped with a host machine, specimen mold, truck, hydraulic control system, and data collection system. By using YDMC-C, the top and two side boundaries were imposed uniform load, respectively; the bottom of the model was fixed on the basement of the machine. The model imposed load gradually until vertical load σ_1 and lateral load both reached 2 MPa; σ_1 corresponded to the depth of 800 m (i.e., mining depth) when generalized average volume-weight of the original rock was selected as 25 kN/m³. Boundary stress condition applied on the physical model was shown as in Figure 2. The model was excavated through 5 steps; each step went forward 8 cm; the lateral pressure coefficient in this process was $\lambda = \sigma_2/\sigma_1 = 1$. In the following steps, the vertical load remained unchanged and increased the lateral load gradually until the model was destroyed to investigate the influence of the lateral stress. The finally vertical load imposed on the physical model was 2 MPa

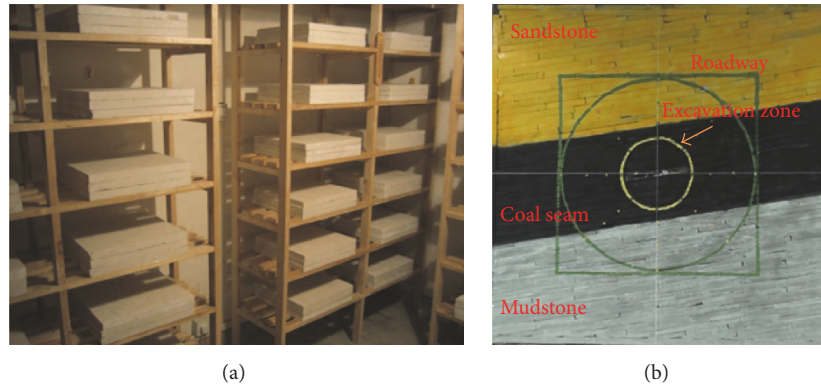


FIGURE 1: Pictures of elementary slabs and the physical model; (a) picture of elementary slabs made of gypsum; (b) picture of the physical model constructed completely.

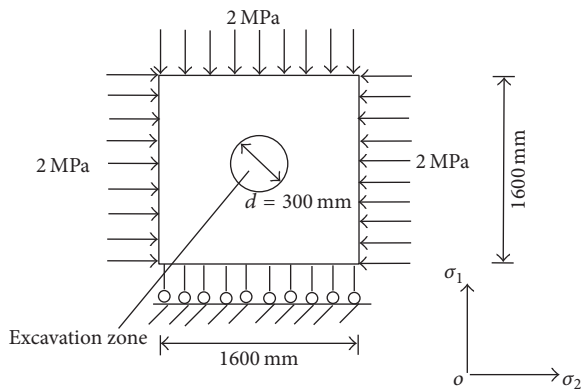


FIGURE 2: Simulated boundary stress conditions during the roadway excavation.

and lateral load was 3.6 MPa before the model ultimately failed. The process of the physical model experiment is illustrated in Table 3.

4. The Failure Process

4.1. Procedural Images Analysis. After excavation and the subsequent stabilization finished, the following fifth-eighth steps of lateral loading were started in turn. The deformation of model occurred and the destruction finally appeared during the process. As shown in Figures 3(a)–3(d), the deformation of the model was small caused by the fifth to seventh loading step. About 1 minute after the eighth loading step, the coal and the mudstone nearby moving towards the left respond to the lower right pressure heads stretched out gradually. Floor heave and shrinkage of right side of the tunnel turned up, as shown in Figure 3(e), and the process lasted about 2 minutes. Then the lower right pressure heads were almost unchanged, but the lower left pressure heads started to run out at a rapid speed. In less than 1 minute, the material in the lower left area moved towards the right, and the left side of the tunnel shrank and floor heave got further development, which can be seen in Figure 3(f). Figure 3(g) shows the rock mass near two flanks and bottom of tunnel

ran into interior and the material in lower part of the model peeled off, and the experiment came to an end.

During the whole test process, the quiet period accounted for the most of the time (0–440 min), and then obvious deformation popped up in about 3 minutes and divided into two parts as mentioned above. Ultimately, deformation of the tunnel was heavy and asymmetric.

4.2. Stacking Sketches Analysis. In order to analyze the deformation and the movement of the model, a concentric circle with three times the radius of the tunnel together with its external square and the whole model outline are painted as the observation frame. Every 45° four equal diversion points are also painted on the segment between the tunnel and the concentric circle along the radius direction and are regarded as displacement observation points, which can be seen in Figure 3. The observation frame and points would be sketched out on the screenshots demonstrated in Figures 3(a)–3(f), respectively. The sketches are superimposed to observe the deformation of the model and the displacement of the observation points, in a qualitative rather than exquisite quantitative manner.

Through the video picture, as Figure 3 shows, the deformation of model can be hardly observed by naked eyes, but it can be found through observation from the stacking sketches shown in Figure 4.

By observing the locus of points in Figure 4(a), in the first destroyed process, the displacement of the rock mass in the upper side and left side of the model is small. The displacement directions of the layers in the upper right side and right side are basically parallel to the strike direction of strata, as the yellow oval frame marked in Figure 4(a) shows. The displacement directions of the monitoring points in down side and lower right side have a certain angle to the strata, as the blue oval frame marked in Figure 4(a) shows, indicating the shearing action would appear along with the displacement; it is a shearing slide motion here. Great change also turns up in the first destroyed process, as shown in Figure 4(b). Large movement takes place in the lower left area and the down side of the tunnel in the second destroyed process, which can be seen through observing the locus of points in Figure 4(b), and has the same trend towards the

TABLE 3: The loading plan of the physical model experiment.

Load level	Simulated depth	Lateral pressure coefficient	Oil pressure		Duration	The cumulative recording time
			Top pressure/MPa	Lateral pressure/MPa		
Preloading			0.4	0.4	12 hours	0 min
1	200 m	1	0.6	0.6	Loading: 15 min Stabilization: 15 min	15 min 30 min
2	400 m	1	1.0	1.0	Loading: 15 min Stabilization: 15 min	45 min 60 min
3	600 m	1	1.6	1.6	Loading: 15 min Stabilization: 15 min	75 min 90 min
4	800 m	1	2.0	2.0	Loading: 15 min Stabilization: 15 min	105 min 120 min
Excavation of the roadway		The first step			Excavation: 14 min Stabilization: 17 min	134 min 151 min
		The second step			Excavation: 22 min Stabilization: 17 min	173 min 190 min
		The third step			Excavation: 37 min Stabilization: 11 min	227 min 248 min
		The fourth step			Excavation: 46 min Stabilization: 17 min	294 min 311 min
		The fifth step			Excavation: 24 min Stabilization: 16 min	335 min 351 min
5	800	1.2	2	2.4	Loading: 17 min Stabilization: 13 min	368 min 381 min
6	800	1.4	2	2.8	Loading: 17 min Stabilization: 13 min	398 min 411 min
7	800	1.6	2	3.2	Loading: 17 min Stabilization: 13 min	428 min 441 min
8	800	1.8	2	3.6	Loading: 4 min	445 min

tunnel, as the dark blue oval frame marked in Figure 4(b) shows. The strata in the lower right side move towards lower right as a whole, as the red oval frame marked in Figure 4(b) shows, and finally peel off, which can be seen in Figure 3(g).

5. Mechanism of Deformation and Failure of the Model

5.1. Analysis Based on Rock Structural Mechanics Model. Taking advantage of rock structural mechanics [19], combining the situation of the model test, the rock structural mechanics models are established, as shown in Figure 5(a). For the same rock layer, the surrounding constraints are elastic because the rock has a certain elastic deformation. q_V and q_N are the loading provided by the constraints, and q_H is the loading provided by hydraulic equipment.

For the same layer, as shown in Figure 5(b), the mechanical analysis of the left side is

$$\begin{aligned} F_x &= P_H \times \cos 10^\circ - P_V \times \sin 10^\circ = f + F_n, \\ F_y &= P_V \times \cos 10^\circ + P_H \times \sin 10^\circ = N. \end{aligned} \quad (2)$$

As shown in Figure 5(c), the mechanical analysis of the right side is

$$\begin{aligned} F_x &= P_H \times \cos 10^\circ + P_V \times \sin 10^\circ = f + F_n, \\ F_y &= P_V \times \cos 10^\circ - P_H \times \sin 10^\circ = N, \end{aligned} \quad (3)$$

where F_x is the horizontal resultant force; F_y is the vertical resultant force; P_H is the horizontal load; P_V is the vertical load; f is the frictional force; F_n is the axial force along the stratum; N is the interlayer pressure.

As F_y is not the same, there would be a certain torque for the layer and the subsequent clockwise movement trend would appear; hence, the left top area of the model is lower than that of the right top area, which can be observed in Figure 3.

The actuating range of these two mechanical analysis models, as P_V has the same effect for these two models, depends on the influencing distance of P_H , which is created by the pressure heads. In no excavated area, the sliding should conquer f and F_n and the sliding space is necessary, which comes from the construction gap and elastic deformation

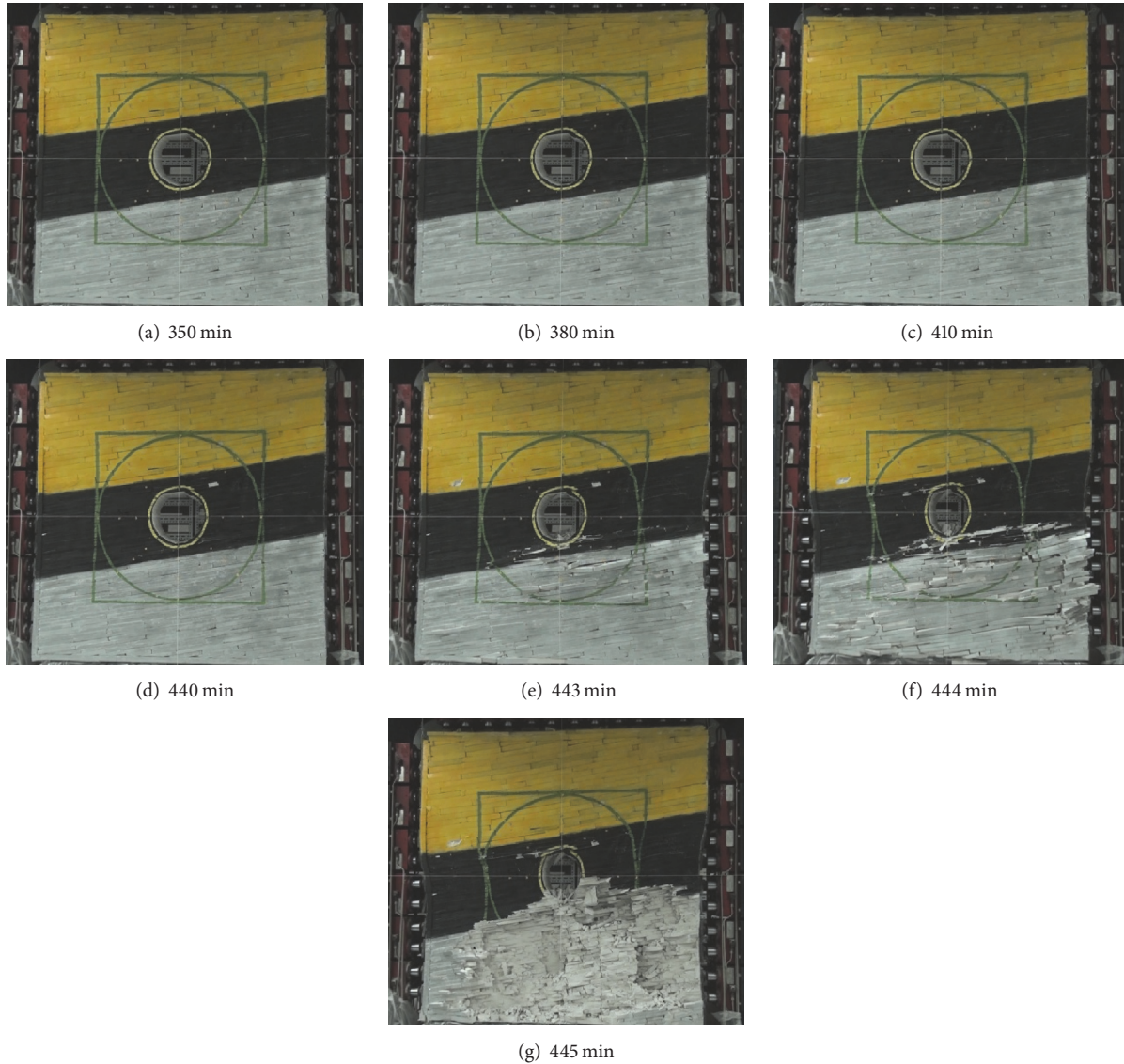


FIGURE 3: Screenshots of test video according to the loading scheme and phenomenon of deformation; (a)–(d) screenshot of the model in stabilization period after the fifth–seventh loading, respectively; (e)–(f) screenshot of large deformation in lower right area and lower left area which occurred after the eighth loading began, respectively; (g) screenshot of the model when it was destroyed.

of rock itself. The value of F_n and f is as the equation, respectively:

$$\begin{aligned} F_n &= E\Delta l, \\ f &= F_y \times \tan \beta, \end{aligned} \quad (4)$$

where E is the elasticity modulus of stratum along the layers; Δl is the deformation of the rock in the actuating range of P_H ; β is the frictional angle of rock interface. When $F_x > f + F_n$, the sliding would happen. F_x of the right side is larger and F_y is smaller than that of the left side, so the layers in the right side are prone to slide, while it is more difficult for the strata in left side and they become more close. As a consequence, the mechanical analysis model of the right side has a broader actuating range than that of the left side. The lower strata are coal seam and mud stone, which have

a lower elasticity modulus than that of the upper sandstone strata, and are easier to slide. Hence, the coal seam and mudstone in the right side of the model are the easiest parts to slide.

After excavation, it turned into bidirectional compression stress state along the tangent direction of the roadway from triaxial stress state in a certain range of surrounding rock. Because there is no supporting measure for the tunnel, F_n equals zero, when the friction between layers was overcome, and the strata move towards the tunnel along the inclined direction of strata. As shown in Figure 3(e), the right side of the tunnel was prone to slide that it is the first place where there was sliding to the roadway. As shown in Figure 4(a), the strata around the roof and floor generated shear failure easily along the shearing slide movement and the displacement directions have a certain angle with the strata, so they are

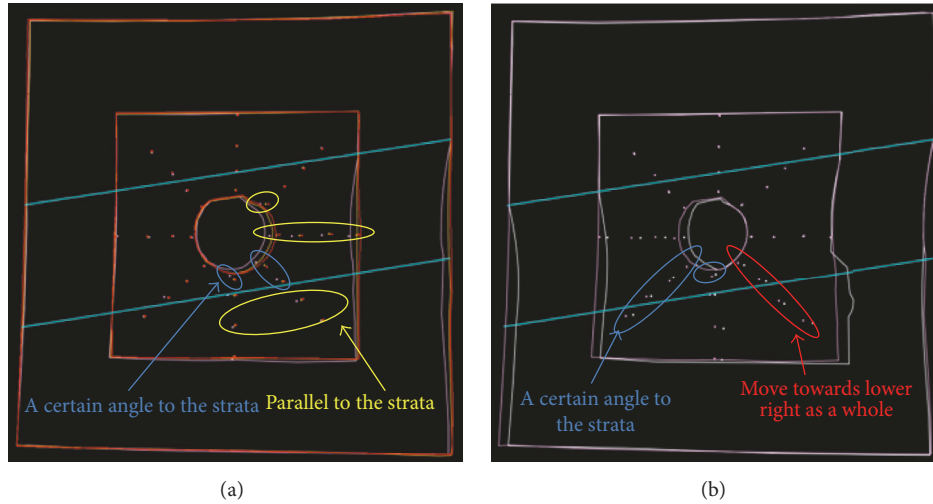


FIGURE 4: Stacking sketches of the images of Figure 3. The lithologic boundaries are drawn by light blue lines; (a) stacking diagram of the sketches of Figures 3(a), 3(d), and 3(e), which is sketched in red, orange, and pink, respectively; (b) the stacking diagram of the sketches of (e) and (f), which is sketched in pink and white line, respectively.

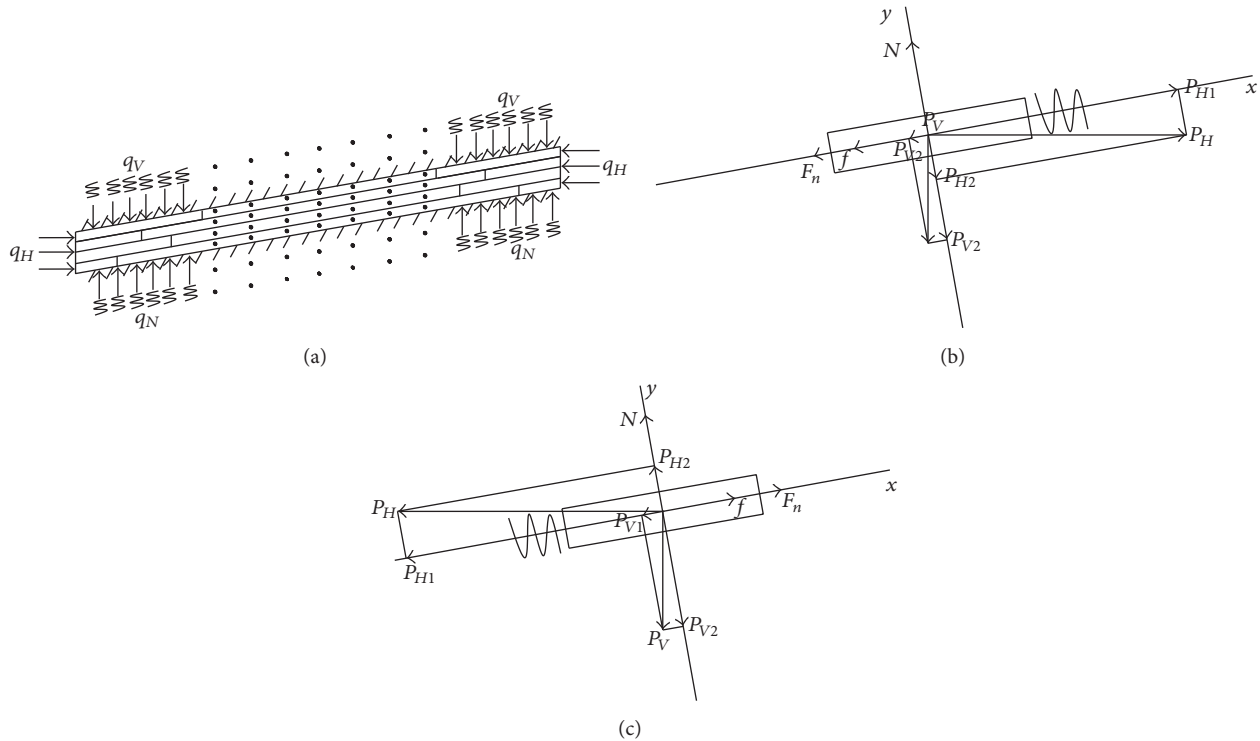


FIGURE 5: Diagrams of rock structural mechanics models; (a) diagram of rock structural mechanics model for the physical model; (b) diagram of rock structural mechanics model for stratum in the left of physical model; and (c) diagram of rock structural mechanics model for stratum in the right of physical model.

the dangerous places. The left side of the model was hard to slide and the upper part of roof was sandstone where shear modulus was high; it was difficult to generate shear failure by shearing sliding and it was easy to slide for the lower coal and mudstone strata, and the shear modulus of them was low; the floor conformed floor heave easily that is consistent with the experimental results as shown in Figure 3(e).

With the growth of the lateral pressure coefficient λ , F_x of the right stratum became smaller than before, while F_y became larger, and it was more easy to slide to give rise to shrinkage of right flank and to cause floor heave through shearing slide of the lower right strata of tunnel. In the meantime, F_y of the stratum in the left side of model got larger, and the strata became compacter than before.

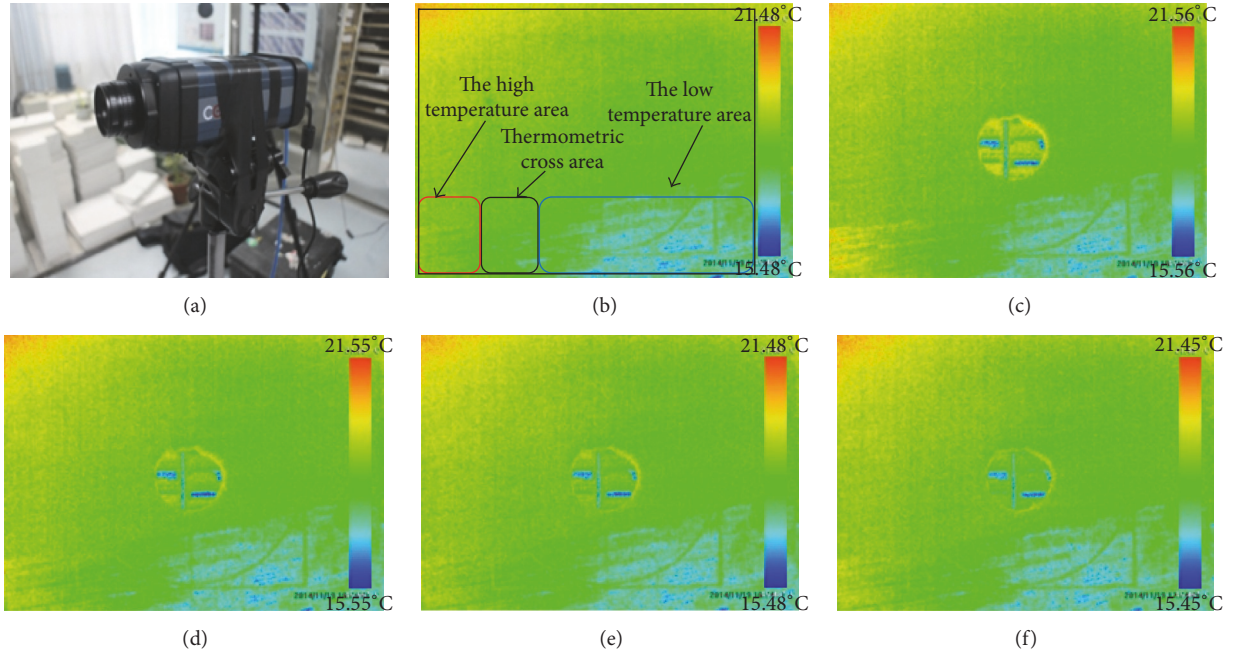


FIGURE 6: Picture of infrared imager and infrared images; (a) picture of infrared thermal imager; (b) infrared image taken after the first loading; (c)–(f) the infrared images taken around the time point of Figures 3(a)–3(d), respectively.

The model was in a stable state during the processes that were from the fifth loading to seventh loading. During the eighth loading, the balance was broken, and shrinkage of the right flank and floor heave occurred. The mechanical strength of material in the down side and lower right side of roadway decreased along the shearing slide and cannot provide enough resistance to the lower left compacted layers moving towards right as a whole, and the second destroyed process, and shrinkage of the left flank and floor heave took place at a rapid speed.

5.2. Infrared Image Analysis. Infrared (IR) thermography, as a nondestructive, remote sensing technique, has been widely used in detection of the onset of unstable crack propagation and/or flaw coalescence for concrete and rock, based on the fact that the heat generation is caused by the intrinsic dissipation due to elasticity and inelasticity of the material under external loading [20, 21]. The variation of temperature consists of three parts [22]:

$$\Delta T = \Delta T_1 + \Delta T_2 + \Delta T_3, \quad (5)$$

where ΔT is the temperature variation in total; ΔT_1 is the change due to the thermoelastic effect, and for plane stress state, if $\Delta\sigma_1 + \Delta\sigma_2 > 0$, $\Delta T_1 > 0$ and vice versa [23]; ΔT_2 is the temperature decrement on account of formation and development of fissures, joints, and fractures, which consume energy; ΔT_3 is the temperature increment from the frictional effect of fissures, joints, and fractures, and it is always positive.

During deformation and failure process of rocks, thermographic imaging records temperature variations on the surface in view and displays it as infrared images with false colors, where a high temperature (in warm color) denotes

shear fracturing from the frictional effects; low temperature (in cool color) represents the tensile fractures indicating permanent plastic damage [24–26]. The analysis of infrared images can provide a further validation and extension of the mechanism of deformation and failure.

The infrared camera CX320 (by Korea) shown in Figure 6(a) was used for monitoring of experimental tests. The IR measurement is performed with the given calibration temperature within the range of -20°C to $+120^\circ\text{C}$ at an accuracy of $\pm 2\%$; minimum measured temperature difference is 0.075°C . Each infrared image contains 384×288 pixels. According to the experience of the physical modeling tests, we just use 370×274 pixels of infrared image for analysis, in order to eliminate the influence of stress boundary. The region of 370×274 pixels of infrared image is marked as a black frame in Figure 5(b). The temperature scale in infrared images is divided equally between the highest and lowest temperature. The infrared images taken around the same time with those of Figures 3(a)–3(d) are shown as in Figures 6(c)–6(f), respectively.

Figure 6(b) shows the temperature distribution of the model surface before excavation. The most outstanding characteristic is a certain width in the left side of the model and is in warm color, which is marked in red frame in Figure 6(b), and the lower right area presents a low temperature state, which is marked in blue frame in Figure 6(b), and there is a transition region between the red frame and blue frame, which is marked in black frame in Figure 6(b). In (5), ΔT_1 should be positive due to the load of the mimetic load of the in situ stress; ΔT_3 is always positive, so the decrement of temperature comes from ΔT_2 . Because the tensile strength of the rock is low and is further below compared to the compressive strength, when bending took shape, tensile

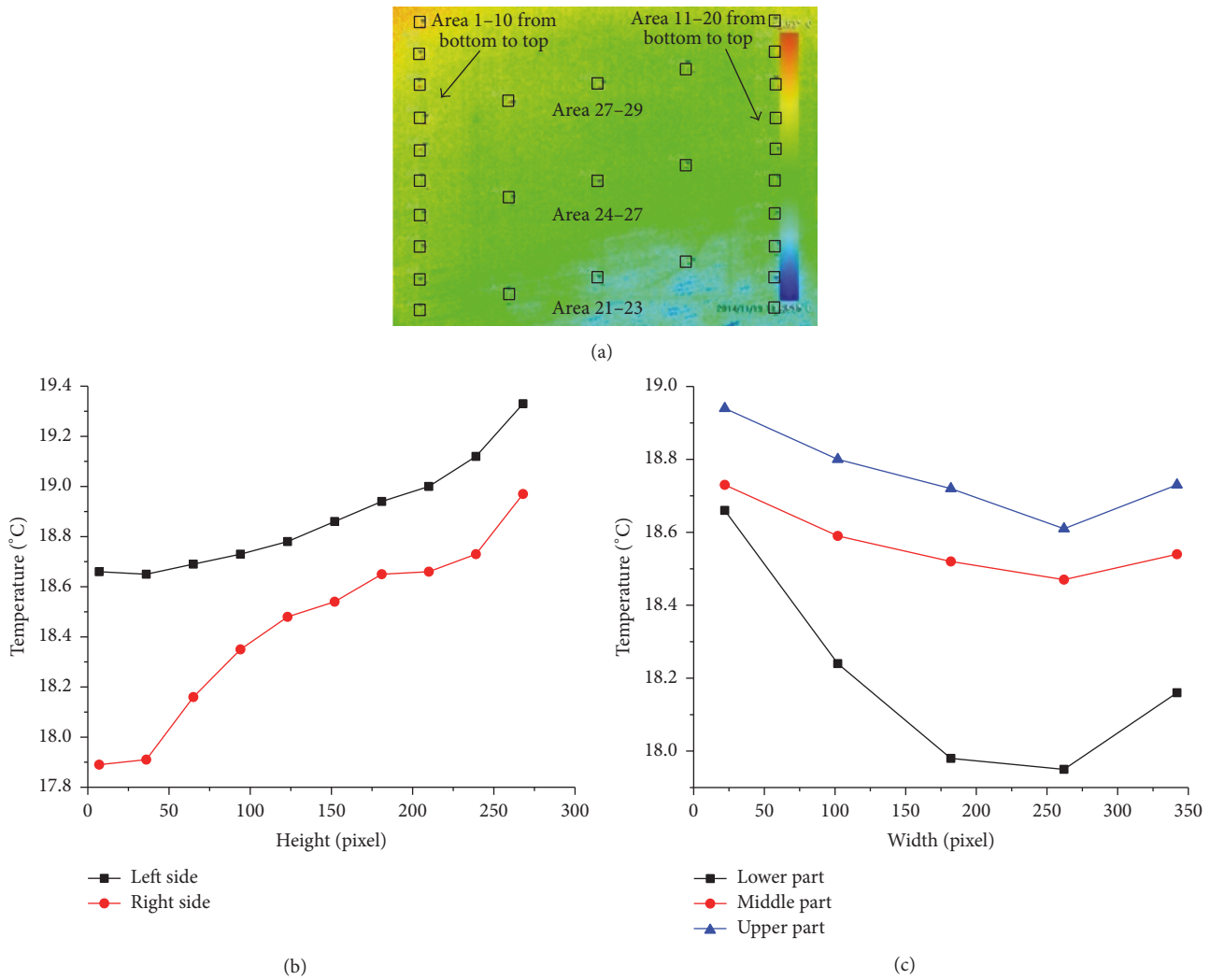


FIGURE 7: Diagrams of arrangement of the temperature ROIs and temperature distribution curves; (a) diagram of arrangement of the temperature ROIs on the infrared image before excavation; (b) diagram of temperature distributions from bottom to top of the model; and (c) diagram of temperature distributions from left to right of the model along the rock tendency.

fractures came along with it. The cold color indicates a certain bending was formed due to the small interlayer pressure in the lower right area and it was easy to produce a certain amount of shape vertical to the strata along with the sliding movement, which was small and was hard to be found by naked eyes. The warm color came from the increment of ΔT_1 and ΔT_3 ; the strata combined closely in this area, and the functions of stress and friction were obvious. Hence, layers contacting closely is a necessary condition for the increment of temperature, and the model was constructed by slabs to form the layered structure of the rock; if the layers are loose, the bending would happen and the temperature would decrease.

As shown in Figure 7(a), the average temperatures of ROI (region of interest) were used to observe the temperature variation of a certain region. $10 \times 10 \text{ pixel}^2$ regions were set along the height of the model in the left side and right side to analyze the temperature variation tendency along the

height; 5 regions with the same size were set along the inclined orientation of the strata in upper part, middle part, and lower part of the model to observe the temperature trend from left to right.

As shown in Figure 7(b), the temperature from bottom to top kept increasing both in the left side and in the right side, which was related to the loading applied to the model. For the strata in the right side, affected by the torque, its temperature maintained growth. The temperature difference between the upper region and lower region reached 0.92°C , because the upper region presented a trend of increase and was in warm color while the trend of the lower area decreased and was in cool color, as shown in Figure 7(a). When coming to the left side, the temperature difference was 0.67°C , and the temperature increased in a gradually increased speed along the shorting of distance to the pressure head. As shown in Figure 7(c), the temperature distribution from left to right both gradually reduced till the fourth area and then got

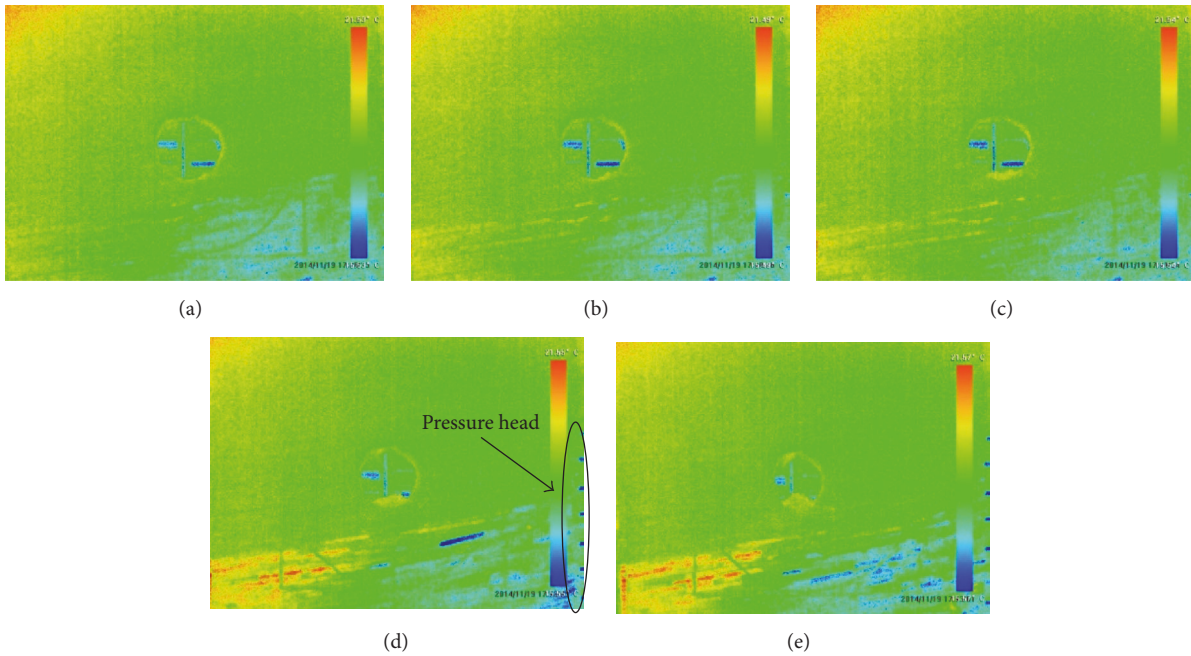


FIGURE 8: Infrared images of the destroyed process; (a)–(e) are infrared images taken after the eighth loading, coming along with the destroyed process.

a growth in the last area. The Saint Venant principle can influence the surrounding of the model as shown in Figure 5. The temperature of model corners is anomaly.

The actuating ranges of the two analysis models as discussed in Section 5.1 can be distinguished by colors, especially in the lower part of the model, where the highest temperature difference reaches 0.71°C , and there was a thermometric cross area which was a transition region connecting the regions of two colors. As shown in Figure 7(a), the width of the cool color was broader than that of the warm color, and the mechanical analysis model of the right side had a broader actuating range than that of the left side, just as Section 5.1 speculated.

After excavation, a circle of red color appeared, as marked in Figure 8(a), because the material was under axial compression of high stress, and shear fracturing came along with it. The overall distribution change was small between the fifth and the seventh load as shown in Figures 6(c)–6(f). Two ROIs of $20 \times 20 \text{ pixel}^2$ were set to observe the temperature variation along the destroyed processes.

Area 1 was pointed in the lower part below the tunnel where the displacement was obvious in the first destroyed process. Area 2 was set in the lower left side of the tunnel where the strata were compacted and moved as a whole in the second destroyed process. The temperature-time curves of two areas were as shown in Figure 9(b). After the beginning of the eighth loading, the region of cool color in lower right area started to contract and it turned into warm color gradually, as shown in Figures 8(a)–8(e), and manifests the original loose layers became compact along the shearing slide movement towards tunnel, and the effect of friction was obvious. The relevant section of the curves both rose up

from the beginning till 94 s, especially that of area 1, and the increment reached 0.30°C . Later on, the temperature of area 1 first rising and then falling off manifests the shearing slide made the strata be compacted first; the falling off showed signs of bending and breakage of slabs when combining the picture of test as shown in Figure 3(e), although it was still in a state of high temperature than before. Although several small sudden drops have been undergone, the temperature of area 2 kept going up basically, indicating that the strata around it are still compact.

The second destroyed process was as short as about 40 s, and the curves had the same trend as the first destroyed process: the curve of area 2 kept increasing basically; the trend of area 1 started to drop after the temperature increasing in the beginning period. The impact of the extrusion from the left strata which have integrated closely as a whole made the broken strata around area 1 become compact and the friction between the fractures and joints was obvious, the temperature rose rapidly, and then the strata became loose gradually and its temperature kept dropping and finally peeled off into pieces, just as shown in Figure 3(g).

6. Conclusions

This paper analyzed the characteristics and mechanisms of deformation based on the physical model test on deep circular roadway in layered rock. The main conclusions were summarized as follows.

The model was finally destroyed by floor heave and shrinkage of two sides. The direction of displacement which caused shrinkage was along the direction of the strata tendency, indicating that the occurrence of shrinkage should

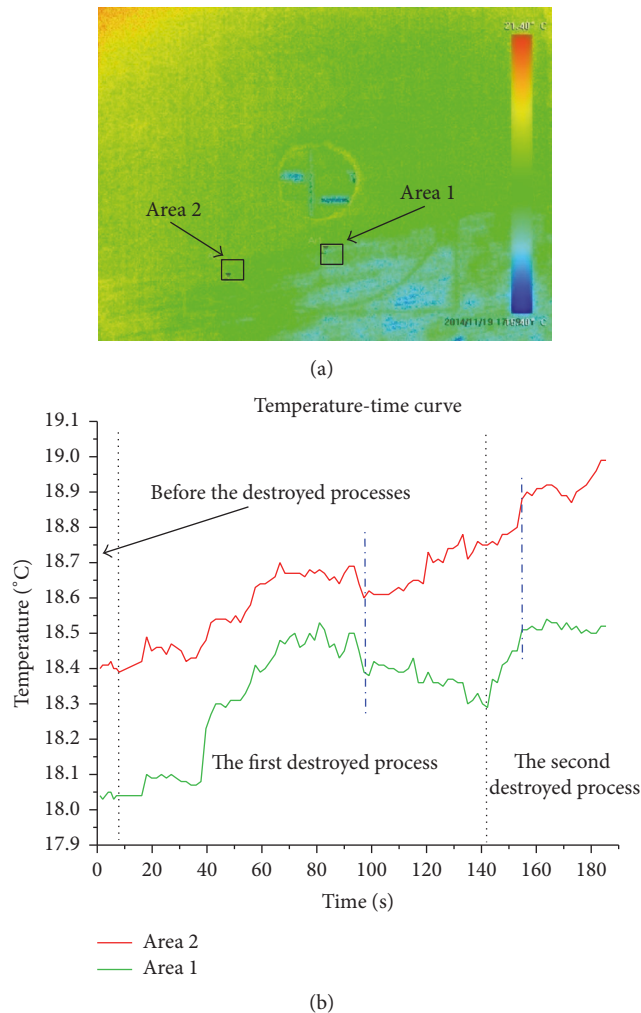


FIGURE 9: Diagrams of the arrangement of the temperature ROIs and temperature variation curves; (a) diagram of the arrangement of the temperature ROIs on the infrared image before the destroyed processes; (b) diagram of temperature variation curves of the ROIs in destroyed process.

only conquer the friction between the layers. There was a certain angle between the direction of displacement which caused floor heave and the layers which manifested the formation of floor heave.

The inclined angle made the stress state of the left side and right side of the model different and affected the trends of movements. The strata in the right side were easy to slide, especially the lower coal seam and mudstone; the strata in right side were hard to slide and become compact. After excavation, combining the increasing lateral pressure coefficient, the movement trends were more obvious; the sliding of the strata in the right side of tunnel triggered the shrinkage; the shearing slide in lower side of tunnel gave rise to floor heave.

Low temperature state indicated tensile fractures generated in lower right area because of bending of layers which was under small interlayer pressure and large trust force. The color of the left area was warm because of result of the frictional influence. The width of the cool color was broader

than that of the warm color along the dip orientation of the strata in the lower part of the model, and the mechanics analysis model of the left side had a broader actuating range.

The temperature trend of the strata in the shearing slide area increased rapidly first and then dropped slowly both in two destroyed processes. In the first process, the increasing indicated the strata became more compact than before along the shearing slide; the dropping manifested the formation of bending and breakage. In the second process, the increasing manifested the frictional function of the fractures and joints under the impact from the left compact layers; the decrement meant the strata became loose which corresponded to the final destroyed phenomenon. The temperature of the lower left area where strata moved as whole kept increasing basically and the increment mainly came from the friction effect.

Conflicts of Interest

The authors declare that they have no conflicts of interest.

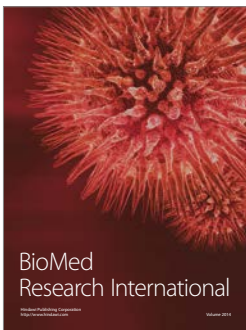
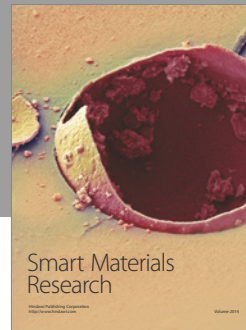
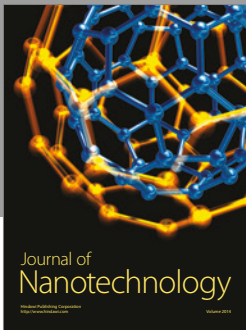
Acknowledgments

This work was supported by the National Key Research and Development Plan of China (2016YFC0600901), the National Natural Science Foundation of China (Grant nos. 51374214, 51134005, and 51574248), the Special Fund of Basic Research and Operating of China University of Mining & Technology, Beijing (Grant no. 2009QL03), and the State Scholarship Fund of China.

References

- [1] H. P. Xie, S. P. Peng, and M. C. He, *Basic Theory and Engineering Practice in Deep Mining*, Science Press, Beijing, China, 2006 (Chinese).
- [2] H. Manchao and X. M. Sun, *Support Design and Construction Guide for Roadway within Soft Rock in China*, Science Press, Beijing, China, 2004 (Chinese).
- [3] H. Manchao, H. P. Xie, S. P. Peng, and Y. D. Jiang, "Study on rock mechanics in deep mining engineering," *Chinese Journal of Rock Mechanics and Engineering*, vol. 24, pp. 2803–2813, 2005 (Chinese).
- [4] H. Manchao, H. H. Jing, and X. M. Sun, *Soft Rock Engineering Mechanics*, Science Press, Beijing, China, 2004 (Chinese).
- [5] J. Wang, Z. Guo, Y. Yan, J. Pang, and S. Zhao, "Floor heave in the west wing track haulage roadway of the Tingnan Coal Mine: mechanism and control," *International Journal of Mining Science and Technology*, vol. 22, no. 3, pp. 295–299, 2012.
- [6] G. Anagnostou and K. Kovári, "Numerical analysis of tunnel floor heaves in swelling ground," in *Proceedings of the International Symposium on Numerical Models in Geomechanics*, pp. 451–456, 1995.
- [7] S. B. Tang and C. A. Tang, "Numerical studies on tunnel floor heave in swelling ground under humid conditions," *International Journal of Rock Mechanics and Mining Sciences*, vol. 55, pp. 139–150, 2012.
- [8] M. R. Islam, D. Hayashi, and A. B. M. Kamruzzaman, "Finite element modeling of stress distributions and problems for

- multi-slice longwall mining in Bangladesh, with special reference to the Barapukuria coal mine,” *International Journal of Coal Geology*, vol. 78, no. 2, pp. 91–109, 2009.
- [9] J. Coggan, F. Q. Gao, D. Stead, and D. Elmo, “Numerical modelling of the effects of weak immediate roof lithology on coal mine roadway stability,” *International Journal of Coal Geology*, vol. 90–91, pp. 100–109, 2012.
- [10] S. Y. Zhu, Z. Q. Jian, H. L. Hou, W. G. Xiao, and P. Yao, “Analytical model and application of stress distribution on mining coal floor,” *Journal of China University of Mining and Technology*, vol. 18, pp. 13–17, 2008.
- [11] W. C. Zhu, J. Liu, C. A. Tang, X. D. Zhao, and B. H. Brady, “Simulation of progressive fracturing processes around underground excavations under biaxial compression,” *Tunnelling and Underground Space Technology*, vol. 20, no. 3, pp. 231–247, 2005.
- [12] H. Manchao, W.-L. Gong, D.-J. Li, and H.-M. Zhai, “Physical modeling of failure process of the excavation in horizontal strata based on IR thermography,” *Mining Science and Technology*, vol. 19, no. 6, pp. 689–698, 2009.
- [13] H. Manchao, X. Jia, W. Gong, and L. Faramarzi, “Physical modeling of an underground roadway excavation in vertically stratified rock using infrared thermography,” *International Journal of Rock Mechanics and Mining Sciences*, vol. 47, no. 7, pp. 1212–1221, 2010.
- [14] H. Manchao, “Rock mechanics and hazard control in deep mining engineering in China,” in *Rock Mechanics in Underground Construction, Proceedings, ISRM International Symposium 2006 4th Asian Rock Mechanics Symposium*, pp. 14–31, 2006.
- [15] G. Weili and W. Jiong, “Thermography analysis of a roadway excavation experiment in 60° inclined stratified rocks,” *International Journal of Rock Mechanics and Mining Sciences*, vol. 60, pp. 134–147, 2013.
- [16] H. Manchao, “Physical modeling of an underground roadway excavation in geologically 45° inclined rock using infrared thermography,” *Engineering Geology*, vol. 121, no. 3–4, pp. 165–176, 2011.
- [17] G. Weili, “Multi-filter analysis of infrared images from the excavation experiment in horizontally stratified rocks,” *Infrared Physics & Technology*, vol. 56, pp. 57–68, 2013.
- [18] G. Weili, P. Yanyan, S. Xiaoming, and H. Manchao, “Enhancement of low-contrast thermograms for detecting the stressed tunnel in horizontally stratified rocks,” *International Journal of Rock Mechanics & Mining Sciences*, vol. 74, pp. 69–80, 2015.
- [19] S. Guangzhong, *Rockmass Structural Mechanics*, Science Press, Beijing, China, 1988 (Chinese).
- [20] M. P. Luong, “Infrared thermovision of damage processes in concrete and rock,” *Engineering Fracture Mechanics*, vol. 35, no. 1–3, pp. 291–301, 1990.
- [21] L. Toubal, M. Karama, and B. Lorrain, “Damage evolution and infrared thermography in woven composite laminates under fatigue loading,” *International Journal of Fatigue*, vol. 28, no. 12, pp. 1867–1872, 2006.
- [22] L. Wu and J. Wang, “Infrared radiation features of coal and rocks under loading,” *International Journal of Rock Mechanics and Mining Sciences*, vol. 35, no. 7, pp. 969–976, 1998.
- [23] N. Harwood and W. M. Cummings, *Thermo Elastic Stress Analysis*, IOP Publishing, Bristol, UK, 1991.
- [24] M. Connolly and Copley, “Thermographic inspection of composite material,” *Materials Evaluation*, vol. 48, pp. 1461–1463, 1990.
- [25] L. Wu, S. Liu, Y. Wu, and C. Wang, “Precursors for rock fracturing and failure—part I: IRR image abnormalities,” *International Journal of Rock Mechanics and Mining Sciences*, vol. 43, no. 3, pp. 473–482, 2006.
- [26] R. Steinberger, T. I. Valadas Leitão, E. Ladstätter, G. Pinter, W. Billinger, and R. W. Lang, “Infrared thermographic techniques for non-destructive damage characterization of carbon fibre reinforced polymers during tensile fatigue testing,” *International Journal of Fatigue*, vol. 28, no. 10, pp. 1340–1347, 2006.



Hindawi

Submit your manuscripts at
<https://www.hindawi.com>

